Contrib Mineral Petrol (2014) 167:992
DOI 10.1007/s00410-014-0992-8

ORIGINAL PAPER

FTIR spectroscopy of Ti-chondrodite, Ti-clinohumite, and olivine in deeply subducted serpentinites and implications for the deep water cycle

Tingting Shen · Jőrg Hermann · Lifei Zhang · José Alberto Padrón-Navarta · Jing Chen

Received: 12 December 2013 / Accepted: 4 March 2014 / Published online: 22 March 2014

Abstract Separated olivine grains from a deeply subducted serpentinized wehrlite (Changawuzi in the western Tianshan ultrahigh-pressure belt, China) were analysed with unpolarized transmission FTIR and the Ti contents were determined using LA-ICP-MS. The major bands in the olivine spectra display striking similarities to Ti-clinohumite and are interpreted as OH in lamellae. The quantification of the water content in lamellae requires calibration of the IR-absorption for such bands. We have obtained a new absorption coefficient for Ti-clinohumite of 0.125+/−0.017 ppm cm^2 based on polarized FTIR measurements on three orthogonal sections through a large single crystal of Ti-clinohumite from Val Malenco, which has a known water content of 1.53 wt%. The resulting water content in olivine using this calibration factor ranges from 440 to 2,600 ppm and correlates positively with the Ti content that ranges from 130 to 1,400 ppm. For the quantification of the water content in Ti-chondrodite and Ti-clinohumite that are associated with olivine, we developed a new method using attenuated total reflectance FTIR spectroscopy. Ti-chondrodite and Ti-clinohumite display similar IR bands at ~3,562, 3,525 and ~3,583–3,586 cm^{-1}. As in olivine, the water content and Ti content correlate in both Ti-clinohumite and Ti-chondrodite, indicating an intergrowth of these minerals, which has been confirmed by TEM analyses. Our results confirm previous suggestions that there is a strong correlation between the Ti content of ultramafic rocks and their capacity to transport water to the deeper mantle in subduction zones beyond conditions where hydrous phases are stable.

Keywords Ti-chondrodite · Ti-clinohumite · Olivine · ATR-FTIR · UHP metamorphism · Tianshan

Introduction

Significant amount of water can be stored as hydroxyl groups in nominally anhydrous minerals (NAMs) such as olivine, clinopyroxene, orthopyroxene and garnet (Bell and Rossman 1992; Bell et al. 1995; Ingrin and Skogby 2000; Berry et al. 2005; Mosenfelder and Rossman 2013a, b). Water in NAMs has a great influence on the physical and chemical properties of the mantle, such as rheology (Hirth and Kohlstedt 1996; Dixon et al. 2004), partial melting (Bell and Rossman 1992; Hirth and Kohlstedt 1996; Karato and Jung 1998; Kovács et al. 2012), transport of major and trace elements, diffusion, elasticity, electrical conductivity (Schlechter et al. 2012), and seismic wave velocity and attenuation (Karato and Jung 1998; Karato 2006; Aizawa et al. 2008). Fourier transform infrared (FTIR) spectroscopy is a convenient method to quantify the concentration of hydrogen associated in NAM's (Paterson 1982; Bell

Communicated by J. Hoefs.

Electronic supplementary material The online version of this article (doi:10.1007/s00410-014-0992-8) contains supplementary material, which is available to authorized users.

T. Shen (✉) · J. Hermann · J. A. Padrón-Navarta
Research School of Earth Sciences, The Australian National University, Canberra, ACT 0200, Australia
e-mail: shentt@pku.edu.cn

T. Shen · L. Zhang · J. Chen
Key Laboratory of Orogenic Belts and Crustal Evolution, MOE, School of Earth and Space Sciences, Peking University, Beijing 100871, China

J. A. Padrón-Navarta
Géosciences Montpellier, CNRS, Univ. Montpellier 2, 34095 Montpellier, France

et al. 2003). Structural information about the site of water incorporation is based on the position of different absorption bands in FTIR studies (Lemaire et al. 2004; Stalder 2004; Berry et al. 2005). Infrared spectroscopy on synthetic olivine has established at least five different mechanisms by which hydrogen is incorporated into the crystal structure: hydrated Si vacancies, hydrated Mg vacancies, Ti-clinohumite-like point defects, Ti-clinohumite lamellae defects and hydrated defects associated with trivalent cations such as Fe^{3+}, Ti^{3+} (Berry et al. 2007; Walker et al. 2007; Kovács et al. 2010).

Experimental studies on water incorporation in olivine have shown that hydrogen solubility and hydroxyl substitution mechanism in olivine at upper-mantle conditions are a function of pressure (Mosenfelder et al. 2006; Tenner et al. 2012), temperature (Zhao et al. 2004; Mosenfelder et al. 2006; Smyth et al. 2006), water fugacity (Costa and Chakraborty 2008; Otsuka and Karato 2011), oxygen fugacity (Grant et al. 2007a) and silica activity (Matveev et al. 2001; Lemaire et al. 2004; Smyth et al. 2006). Experimental studies are generally conducted under water-present conditions and thus cannot be directly applied to the question of how much water is stored in the lithospheric mantle. To address this, several studies have investigated how much water is stored in olivine and pyroxene from mantle xenoliths (Bell et al. 2003; Grant et al. 2007b; Li et al. 2008; Xia et al. 2010; Soustelle et al. 2010; Schmädicke et al. 2013; Denis et al. 2013). Using this approach, it must be evaluated how much of the water can be retained in the NAM's during the transport to the Earth's surface when they are incorporated into hot magmas (Demouchy et al. 2006; Peslier and Luhr 2006; Peslier et al. 2008; Denis et al. 2013; Padrón-Navarta et al. 2014).

In contrast to the vast number of studies on mantle xenoliths, there are only a few studies addressing the water transport in olivine at conditions relevant for subduction zones. Water recycling in subduction zones is primarily related to the breakdown of hydrous phases (Schmidt and Poli 1998). Serpentine and chlorite in ultramafic rocks, either in the subducted slab or in the mantle wedge, are a major host for water in subduction zones (Ulmer and Trommsdorff 1995; Spandler and Pirard 2013). However, little is known about the capacity and mechanisms of retaining water in olivine beyond the breakdown of these hydrous phases during such low-temperature, high-pressure metamorphism. A few studies highlighted the importance of lamellar structures in olivine related to an intergrowth of humite minerals and olivine down to atomic levels as a mechanism of water incorporation in olivine (Risold et al. 2001; Hermann et al. 2007; López Sánchez-Vizcaíno et al. 2005, 2009). Therefore, there is a potential link between water incorporation and the minor element Ti, which is known to stabilize humite minerals such as Ti-clinohumite and Ti-chondrodite (Weiss 1997).

In this study, we investigated the mechanisms of water (i.e. OH) incorporation into olivine from an unusual metamorphosed wehrlite in the Tianshan UHP belt, China. Olivine is associated with Ti-clinohumite and Ti-chondrodite providing an opportunity to directly study the relationship between hydrous defects in olivine with Ti-clinohumite and Ti-chondrodite. Based on their stoichiometric formula, Ti-clinohumite [$4((Mg, Fe)_2SiO_4)(Mg_{1-X}, Ti_X)O_{2X}(OH, F)_{2-X}$] and Ti-chondrodite [$2((Mg, Fe)_2SiO_4)(Mg_{1-X}, Ti_X)O_{2X}(OH, F)_{2-2X}$, $X = 0$–0.5 refers to mole of Ti content] contain 1.4–2.8 and 2.5–5.2 wt% H_2O. The huge range of water concentrations from olivine to Ti-chondrodite makes it impossible to measure all minerals with the same FTIR setup. To overcome this problem, we have developed a FTIR method for humite minerals that make use of attenuated total reflectance (ATR). The second challenge is related to the quantification of water in humite lamellae in olivine, which requires a new calibration of the absorbance. In this paper, we present first the technical developments to address these problems. The techniques are then applied to the Tianshan serpentinites to address the questions of how and how much water is incorporated in olivine from deeply subducted ultramafic rocks and to investigate potential links between Ti contents of rocks and the capacity to host water beyond the breakdown of hydrous phases.

Sample description

A centimetre-sized Ti-clinohumite from Val Malenco (TiCl-M), N-Italy was used for the technical developments. TiCl-M is part of sample 93-8-4 that has been described in detail by Weiss (1997) and derives from a vein consisting of Ti-clinohumite, olivine, magnetite, antigorite, chlorite and minor calcite. The vein crosscuts serpentinites with the assemblage diopside + antigorite + olivine + chlorite + magnetite that formed during the main Alpine upper greenschist to lower amphibolite facies metamorphism (Trommsdorff and Evans 1974, 1980). The composition of the studied 5 cm large Ti-clinohumite is given in Table 1.

The investigated sample on which we applied the new developments comes from the Changawuzi ultramafic complex, western Tianshan ultrahigh-pressure belt, China. The western Tianshan metamorphic rocks are exposed in a 200-km-long, Late Palaeozoic orogenic belt between the Yili-Central Tianshan and Tarim plates (Fig. 1 of Zhang et al. 2013). The UHP metamorphic belt contains eclogites, blueschists, garnet-mica schists, greenschists and dismembered metaophiolites (Li et al. 2007; Lü et al. 2008). The Changawuzi ultramafic complex constitutes the main

Table 1 Composition of Ti-clinohumite from Malenco and Ti-clinohumite, Ti-chondrodite, Olivine from Changawuzi, Tianshan, China

Mineral	TiCl-M*		TiCh-C#		TiCl-C#		Ol-C			
							Clear olivine		Yellow olivine	
Analysis number	$n = 22$	SD	$n = 33$	SD	$n = 24$	SD	$n = 38$	SD	$n = 17$	SD
SiO_2	35.93	1.12	33.72	0.67	36.84	0.68	40.88	0.64	40.19	0.59
TiO_2	5.51	0.14	6.80	0.86	2.64	0.79	0.02	0.02	0.21	0.10
Al_2O_3	0.09	0.16	0.02	0.04	0.04	0.07	0.03	0.06	0.04	0.09
Cr_2O_3	0.01	0.02	0.07	0.04	0.03	0.03	0.02	0.02	0.02	0.02
FeO	10.47	0.77	7.96	0.34	7.77	0.37	8.20	0.34	8.10	0.45
MnO	0.64	0.08	0.40	0.05	0.36	0.07	0.33	0.04	0.35	0.04
MgO	46.53	0.98	47.82	0.73	49.82	0.87	50.40	0.55	50.40	0.44
CaO	0.02	0.04	0.02	0.02	0.01	0.01	0.02	0.02	0.02	0.03
Na_2O	0.00	0.00	0.01	0.01	0.01	0.01	0.01	0.01	0.00	0.01
K_2O	0.00	0.01	0.01	0.01	0.01	0.01	0.01	0.01	0.00	0.01
NiO	0.19	0.08	0.21	0.06	0.24	0.05	0.35	0.04	0.33	0.04
H_2O^{cal}	1.53	0.03	3.48		2.18					
Total	100.90	1.60	100.51	0.80	99.94	1.16	100.27	0.97	99.67	0.72
Si	3.92	0.07	2.01	0.03	3.99	0.03	0.99	0.01	0.98	0.01
Ti	0.45	0.01	0.30	0.04	0.21	0.06	0.00	0.00	0.00	0.00
Al	0.01	0.02	0.00	0.00	0.00	0.01	0.00	0.00	0.00	0.00
Cr	0.00	0.00	0.00	0.00	0.00	0.00	0.00	0.00	0.00	0.00
Fe^{2+}	0.96	0.08	0.40	0.02	0.70	0.03	0.17	0.01	0.17	0.01
Mn	0.06	0.01	0.02	0.00	0.03	0.01	0.01	0.00	0.01	0.00
Mg	7.58	0.06	4.25	0.04	8.03	0.08	1.83	0.02	1.84	0.02
Ca	0.00	0.00	0.00	0.00	0.00	0.00	0.00	0.00	0.00	0.00
Na	0.00	0.00	0.00	0.00	0.00	0.00	0.00	0.00	0.00	0.00
K	0.00	0.00	0.00	0.00	0.00	0.00	0.00	0.00	0.00	0.00
Ni	0.02	0.01	0.01	0.00	0.02	0.00	0.01	0.00	0.01	0.00
OH	1.11	0.02	1.39	0.08	1.57	0.13				

* Data of sample 93-8-4 from Weiss (1997), p116

\# TiCh and TiCl were normalized on the basis of 7 cations, 18 charges; 13 cations, 34 charges, respectively

part of the western Tianshan ultramafic rocks, which are considered to be a relic of Palaeozoic oceanic crust in the southern margin of the Yili-Central Plate. Serpentinized peridotites (such as wehrlite, harzburgite and dunite) and minor lenses of rodingite and eclogite are the main rock types in this ultramafic complex (Li et al. 2007; Shen et al. 2012). Previous studies indicated that the serpentinized peridotites, eclogites and the surrounding pelitic rocks experienced HP/UHP metamorphic conditions of ~460–630 °C and pressures ranging from 2.5 to 5.0 GPa during subduction (Zhang et al. 2002, 2003; Lü et al. 2009, 2012a, b; Tian and Wei 2013).

The studied sample C11107 is a serpentinized wehrlite containing a peak mineral assemblage of Ti-chondrodite + olivine + antigorite + diopside + chlorite + magnetite, which is in agreement with the metamorphic conditions derived from other rock types. Ti-chondrodite (TiCh-C) displays a deep orange colour in thin section and is commonly surrounded by Ti-clinohumite (TiCl-C) showing a more yellow–orange colour (Fig. 1a, b). Both humite minerals display straight grain boundaries with neighbouring antigorite and also contain antigorite inclusions, indicating that they grew within the antigorite stability field. Olivine occurs as patchy grains ranging in size from a few hundred microns to more than 2 mm. Olivine commonly displays a clear colour but in many places it turns to yellow due to patchy intergrowth with Ti-clinohumite (Fig. 1c). Occasionally, the intergrowth is in the form of sharp Ti-clinohumite lamellae within olivine (Fig. 1c, d) in a similar way to the ones described by López Sánchez-Vizcaíno et al. (2005). Average compositions of Ti-chondrodite, Ti-clinohumite, clear and yellow olivine are given in Table 1.

Analytical techniques

Separation of olivine (Ol-C, olivine from China), Ti-clinohumite (TiCl-C, Ti-clinohumite from China) and Ti-chondrodite (TiCh-C, Ti-chondrodite from China) was conducted at the Geological Survey at Langfang, Hebei Province, China. Mineral extraction was processed by

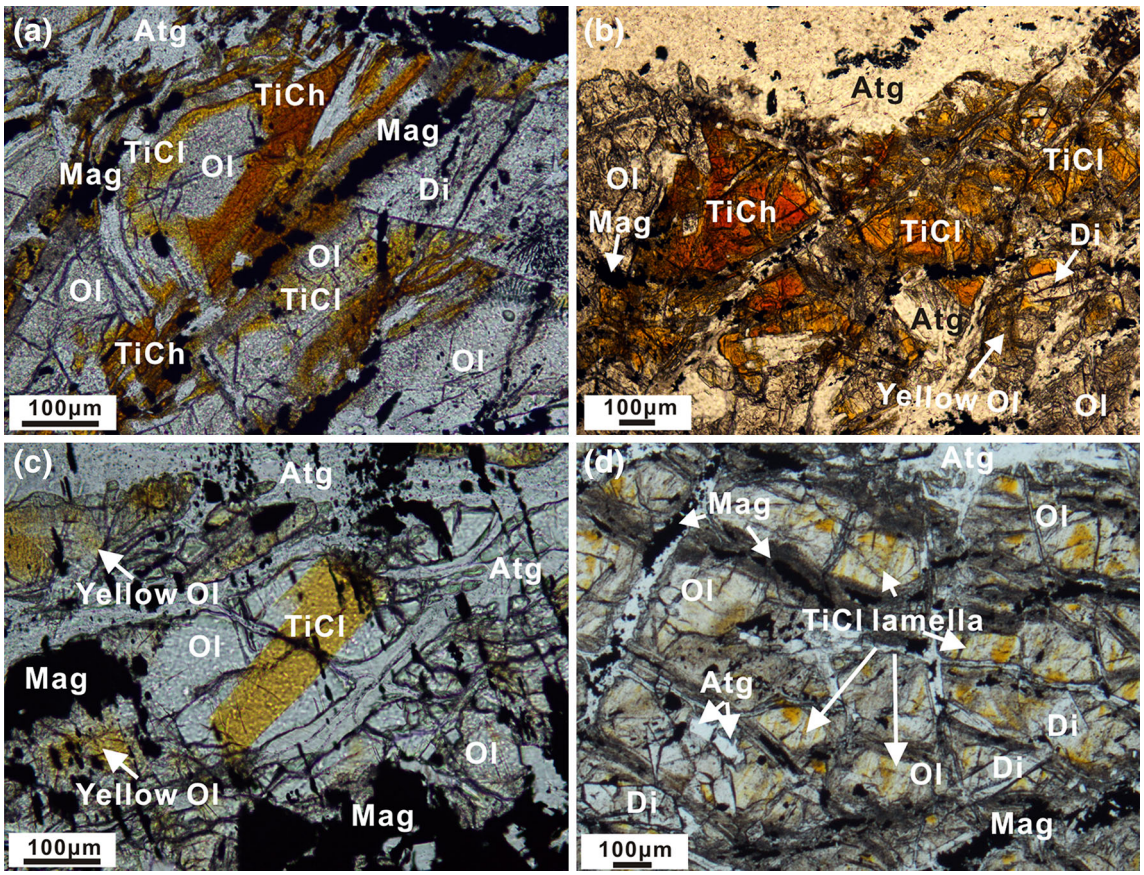

Fig. 1 Photomicrographs showing mineral assemblage and textural relationships in the serpentinized wehrlite, Changawuzi, Tianshan, China. **a** Tight intergrowth of Ti-chondrodite (TiCh), Ti-clinohumite (TiCl) and olivine (Ol). Antigorite (Atg) blades are in textural equilibrium with olivine and humite minerals. **b** A core of Ti-chondrodite is surrounded by Ti-clinohumite and olivine within an antigorite matrix. **c** Ti-clinohumite lamellae included in clear olivine. *Yellow* olivine occurs in patches and has higher Ti content than clear olivine. **d** Ti-clinohumite as patches or lamellae in olivine associated with antigorite, diopside (Di) and magnetite (Mag)

magnetic separation after crushing a clean block of rock using a corundum jaw crusher and then handpicked under a microscope. The grain size of TiCl-C and TiCh-C is up to 500 μm, whereas clean olivine grains are typically ~200 μm in diameter.

Fourier transform infrared (FTIR) and attenuated total reflection (ATR)-FTIR spectroscopy analyses were carried out at the Research School of Earth Science, the Australian National University. A Bruker Tensor 27 FTIR spectrometer with a KBr beamsplitter and globar source was used connected to a Hyperion 1,000 microscope with an MCT detector cooled with liquid nitrogen. For polarized measurements, a KRS-5 polarizer was used. During each analysis, a polished wafer or single mineral grains were placed within a dry-air purged area of the microscope to minimize interference with atmospheric water and carbon dioxide. Analyses were made with an 80 × 80-μm^2 square aperture. Spectra were recorded in the range of 600–4,500 cm^{-1} with a resolution of 4 cm^{-1} by averaging 64 scans. The atmospheric compensation tool and background subtraction using the concave rubber band algorithm with four iterations and 64 baseline points of the OPUS® software were used after acquisition. For quantification of the water content, the area under the OH bands was integrated using the integration toolbar of the OPUS® software. The region of integration is usually from 3,000 to 3,590 cm^{-1} for Ti-clinohumite and Ti-chondrodite, from 3,300 to 3,620 cm^{-1} for olivine. The choice of baseline can influence the integration. We found that using the above described background correction provided the most coherent and reproducible results. Multiple analyses of the same grains have shown that the uncertainty in integrated absorbance for an individual analysis is ~5 %.

Attenuated total reflectance (ATR) FTIR was used to analyse the hydrous minerals Ti-chondrodite and Ti-clinohumite. The ATR objective consists of a cone-shaped Germanium crystal (refractive index of 4) with a flat tip of 50 μm diameter that is pressed onto the sample. The aperture in the microscope was fully opened resulting in an effective spot size of 32 μm. The incident beam hits the sample at an angle of about 30°, then an evanescent wave enters the sample, which is generated due to quantum

mechanical constraints when the total internal reflection of the light takes place. The signal of the evanescent wave is collected by the same Germanium crystal and guided back to the detector in a single reflection ATR (Electronic Appendix Fig. 1). This technique is highly advantageous for samples with high water contents such as hydrous minerals or glasses. The short path length in the order of a micron (see below) of the IR beam through the sample prevents saturation of the absorbance signal. Lowenstern and Pitcher (2013) provide a detailed description of the ATR method applied to hydrous glasses. A second advantage of the ATR method is that only one polished surface is needed for analyses, making it easy to apply to grain mounts. Compared with transmission FTIR spectroscopy, the absorbance intensity for ATR spectra are very low. During ATR measurements, the penetration depth of the evanescent wave depends on the wavenumber and dispersion effects can lead to small shifts in band positions. We performed an extended ATR correction from the OPUS® software to the ATR spectra such that the position and intensity of the absorption bands are similar to those of the spectra acquired in transmission mode. Except that, the acquisition parameters and data evaluation procedure for the ATR-FTIR were the same as for the unpolarized measurements in transmission mode.

Mineral analyses were performed on a JXA-8800R electron microprobe at Peking University operated at 15 kV acceleration voltage, 20 nA beam current. Natural jadeite (Si), forsterite (Mg), haematite (Fe), albite (Na, Al), rutile (Ti), rhodonite (Mn) and sanidine (K) served as standards.

The concentration of Ti in Ti-clinohumite and Ti-chondrodite were determined by a JEOL 6400 SEM (Centre of Advanced Microscopy, ANU) with EDS operating at 15 kV and a focussed beam of 1 nA using a variety of silicates and metals as calibration standards. For the 100 s of counting, the detection limit of TiO_2 is typically at 0.2 wt%, well below the measured values.

The Ti concentration of olivine, Ti-clinohumite and Ti-chondrodite was also measured by laser ablation inductively coupled plasma mass spectrometry (LA-ICP-MS) at the Research School of Earth Science, the Australian National University. Samples were placed in an in-house constructed HelEX ablation cell and ablated by a Compex 110 Excimer laser operating at 5 Hz and output energy of 4–5 mJ at the sample surface. The ablated material was transported to an Agilent 7700 ICP-MS by a He–Ar carrier gas. Individual olivine crystals that were previously analysed by FTIR were mounted in epoxy for analysis. A spot size of 81 and 105 μm was used. NIST 610 glass was used as the external standard (values from GeoRem database as of Dec09) and Si previously determined by electron microprobe or SEM–EDS as the internal standard. All LA-ICP-MS data were processed using iolite in Igor Pro (produced by Hellstrom et al. www.iolite.org.au). BCR glass was used as secondary standard and the Ti concentrations were within 5–10 % of the value published in the GeoRem database as of Dec09.

TEM images were acquired by a Hitachi H-9000NAR housed at the Electron Microscopy Laboratory, Peking University, China, employing an acceleration voltage of 300 kV. The selected humite grains were extracted from a double polished thin section with the thickness of less than 25 μm using a nickel ring. The TEM foil was obtained by ion-beam milling of the extracted sample.

Development of quantitative FTIR analyses of humite minerals using ATR mode

For the determination of water contents in Ti-clinohumite, Ti-chondrodite and olivine, the specific absorption coefficient of Ti-clinohumite and the path length of the IR beam through the samples using ATR-FTIR are both needed. The Val Malenco Ti-clinohumite single crystal (TiCl-M) was used for this purpose. The crystal was cut in half. One half was then cut into three random, but orthogonal-oriented pieces (Electronic Appendix Fig. 2) and prepared into double polished wafers that were thoroughly cleaned in acetone. The thickness of the three wafers, 24 μm (Section-1), 30 μm (Section-2) and 30 μm (Section-3), respectively, were determined with a Mitutoyo machinist's digital indicator, which is nominally accurate to within 2 μm. The other half of the single crystal was crushed into small pieces, then mounted in epoxy in random orientation and polished for ATR-FTIR measurements.

Absorption coefficient

From the three orthogonal-oriented sections polarized IR spectra were recorded in transmission mode. The sample was rotated through a 180° segment with 15 measurements taken in 12.9° steps. All the measured spectra are presented in Fig. 2, Electronic Appendix Figs. 3 and 4. The absorbance for Ti-clinohumite includes sharp bands at 3,562(3), 3,525(4), and a broader band at ~3,414–3,385 cm^{-1}. The bands are changing their intensity with rotation in each section. The positions of the sharp bands at high wavenumber remain constant with the stage rotation, whereas the broad band at lower wavenumber shows a shift in the main band position from 3,412 to 3,393 cm^{-1}. This suggests that the broad band is composed of at least two bands with very close OH-stretching vibrations that have a different polarisation resulting in a changing intensity of each band during the rotation of the sample.

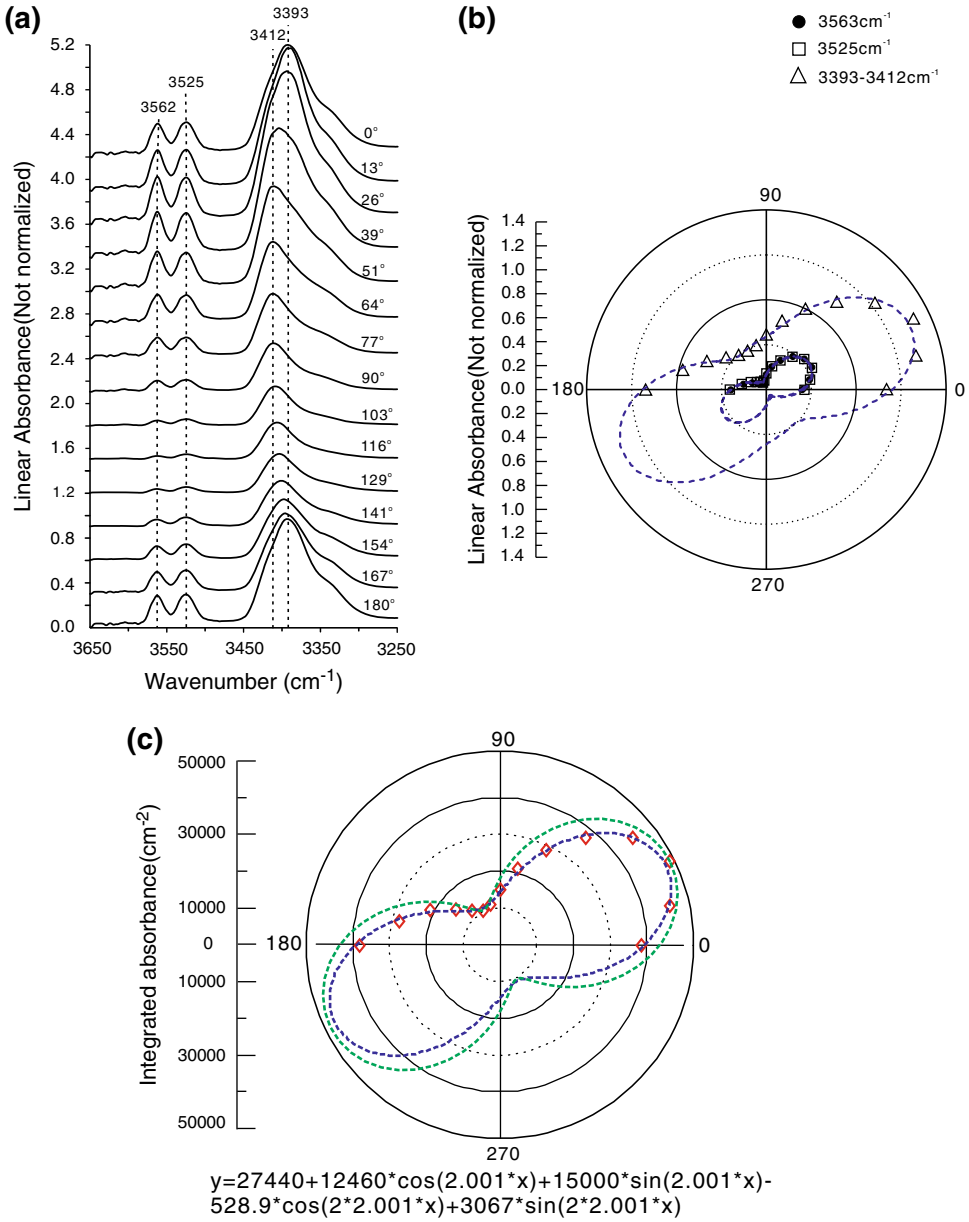

Fig. 2 Polarized transmission FTIR results of a Ti-clinohumite from Val Malenco (TiCl-M) in Section-1. **a** The incident IR beam was normal to the polished wafer, and rotated by 12.9° after each measurement. All the measurements were made within 180°. Note that the position of bands at 3,562 and 3,525 cm^{-1} remain constant, but there is an apparent band shift from 3,393 to 3,412 cm^{-1}. The intensity of all the bands changed with orientation. **b** The angular intensity distribution for the linear absorbance of the main bands (*filled dots*, *squares* and *triangles*). The *three blue dashed lines* represent best-fit Fourier transform functions to the observed data. **c** The distribution of integrated absorbance (between 3,000 and 3,590 cm^{-1}) of TiCl-M in Section-1 (*red diamonds*). The *purple dashed line* represents the best-fit Fourier transform function to the observed data, whereas the *green dashed curve* shows the theoretical angular distribution according to the formula: $A(\theta) = A_{pol}^{\max} \cos^2\theta + A_{pol}^{\min} \sin^2\theta$ ($A_{pol}^{\max} = 50{,}100$; $A_{pol}^{\min} = 11{,}100$). The best-fit function shown at the bottom of the graph serves to calculate maximum and minimum integrated absorbance that has been used to determine the total absorbance given in Table 2. Graphs of the other two sections are shown in the Electronic Appendix Fig. 3, 4

Based on the altered Beer–Lambert's law, the absorbance in isotropic material is linearly dependent on the concentration of the absorber and on the thickness of the sample

$$A = c \times t/k \quad (1)$$

where A is the absorbance, k is the absorption coefficient of the material, c is the water content in ppm H_2O by weight (μg/g) and t is the thickness of the sample in cm. For anisotropic materials, 'A' is the total absorbance of the absorption indicatrix: $A_{\text{total}} = A_x + A_y + A_z$. As it is difficult and time-consuming to get anisotropic materials exactly cut along the main absorption axes, the total absorbance can also be accomplished by polarized measurement of principal directions in three randomly oriented but orthogonal crystal sections. In these sections, the maximum and minimum absorbance is then determined and the total absorbance is calculated by $A_{\text{total}} = \sum_{i=1}^{3} (A_{\max,i} + A_{\min,i})/2$ (Libowitzky and Rossman 1996). The total integrated absorbance of TiCl-M has been calculated based on the maximum and minimum integrated absorbance of each section (Fig. 2; Table 2) and the measured thickness of each wafer. It is interesting to note that the angular dependence of the integrated absorbance of the complex bands in clinohumite slightly deviates from the simple theoretical behaviour of a single peak. However, there is no difference for the maximum and minimum absorbance, which is used in the calculation of the total absorbance. For the bands between 3,000 and 3,590 cm^{-1} the total integrated normalized absorbance is

Table 2 Integrated absorbance from polarized transmission measurements of three orthogonal TiCl-M wafers and from unpolarized ATR-FTIR measurements

Sample	Integrated absorbance (calibrated to 1 cm)
Section 1 (3,590–3,000 cm^{-1})	
Min	11,100 cm^{-2}
Max	50,100 cm^{-2}
(Max + Min)/2	30,600 cm^{-2}
Section 2 (3,590–3,000 cm^{-1})	
Min	11,100 cm^{-2}
Max	72,800 cm^{-2}
(Max + Min)/2	41,950 cm^{-2}
Section 3 (3,590–3,000 cm^{-1})	
Min	20,700 cm^{-2}
Max	79,900 cm^{-2}
(Max + Min)/2	50,300 cm^{-2}
Total absorbance (calibrated to 1 cm)	122,850 cm^{-2}
Total absorbance of ATR-FTIR	15.3 cm^{-1}
Path length d of ATR-FTIR	1.25 μm

Typical error for the integrated absorbance is 5 %

122,850 cm^{-2} (Table 2). The molar fraction of Ti (X_{Ti}) for TiCl-M is 0.45, and there is no detected F in the crystal (Table 1), resulting in a stoichiometric water content of 1.53 wt% H_2O (Table 1). This value is slightly lower than the 1.71 wt% H_2O determined by IR-LECO spectroscopy using the combustion method (Weiss 1997). The small discrepancy can be explained by the minor alteration/inclusions of the hydrous minerals chlorite and antigorite. Using Eq. (1), the absorption coefficient of Ti-clinohumite is then calculated to be $k_{TiCl} = 0.125$ ppm cm^2. Assuming an error of 5 % for the integrated absorbance and thickness for each section as well as for the water content in TiCl-M, the resulting error on k_{TiCl} is 0.017 when errors are added in quadrature.

Unpolarized ATR-FTIR measurement of randomly oriented TiCl-M

A polished epoxy mount of 25 randomly oriented grains of TiCl-M was analysed with the ATR objective. Each grain was measured three times. The linear absorbance of all the bands is in the range of 0.007–0.088 and easily resolved from the background. Figure 3 shows the average unpolarized absorbance of all measurements together with all the spectra measured. If the maximum polarized linear absorbance is smaller than ~0.3, or the maximum unpolarized linear absorbance is less than 0.15, the total absorbance of an anisotropic material can be determined from the average of unpolarized measurements of randomly oriented grains by the simple formula:

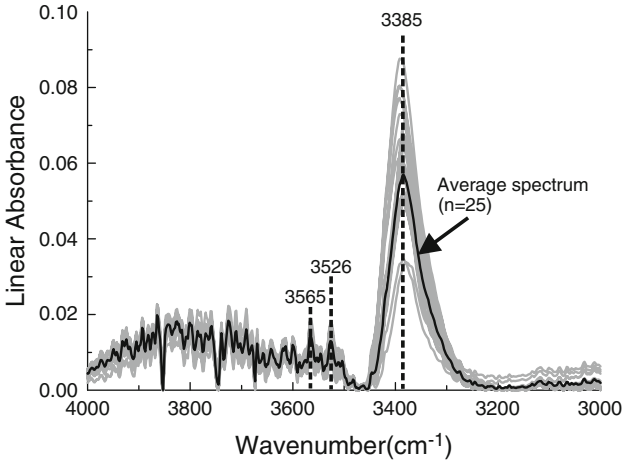

Fig. 3 Unpolarized linear absorbance of TiCl-M measured by ATR-FTIR. The average IR spectrum (*black solid line*) was calculated based on 25 measurements (*grey solid lines*)

$A_{total} = A_{unpol} * 3$ (Kovács et al. 2008; Sambridge et al. 2008). The integrated A_{total} of TiCl-M by ATR-FTIR is 15.3 cm^{-1} (Table 2). For the 25 unpolarized measurements on randomly oriented TiCl-M, the error in total absorbance should be less than 10 % (Sambridge et al. 2008). Using Eq. (1) for both the polarized transmission and the unpolarized ATR measurements returns the following relationship: $A_{pol\ FTIR}/A_{ATR} = t_{pol\ FTIR}/t_{ATR}$. This yields an effective path length of the IR beam through the Ti-clinohumite crystal of 1.25 μm. The effective path length is a bit more than double the depth of penetration (d_p) of the IR beam, which is ~0.48 μm at 3,000 cm^{-1} and 0.76 μm at 1,800 cm^{-1} calculated based on Eq. (2).

$$d_p = \frac{\lambda}{2\pi n_{IRE}\sqrt{\sin^2\theta - \left(\frac{n_{smp}}{n_{IRE}}\right)^2}} \quad (2)$$

λ is the wavelength of light (m), n_{IRE} is the refractive index of the ATR crystal (4 for Germanium), n_{smp} is the refractive index of the sample (1.67 for Ti-clinohumite) and θ is the angle of the incident light in degrees (30° in this study).

In the following, we use the empirically determined path length of 1.25 μm for the quantification of water in Ti-clinohumite and Ti-chondrodite.

Ti-clinohumite, Ti-chondrodite and olivine from Tianshan rocks

In a first attempt to measure the IR spectra of olivine, Ti-chondrodite and Ti-clinohumite in the Tianshan rocks, we prepared a 300-μm-thick double polished wafer of the sample. However, we were unable to measure clean spectra of olivine because of minor inclusions/alterations of serpentine minerals. On the other hand, the absorption of the

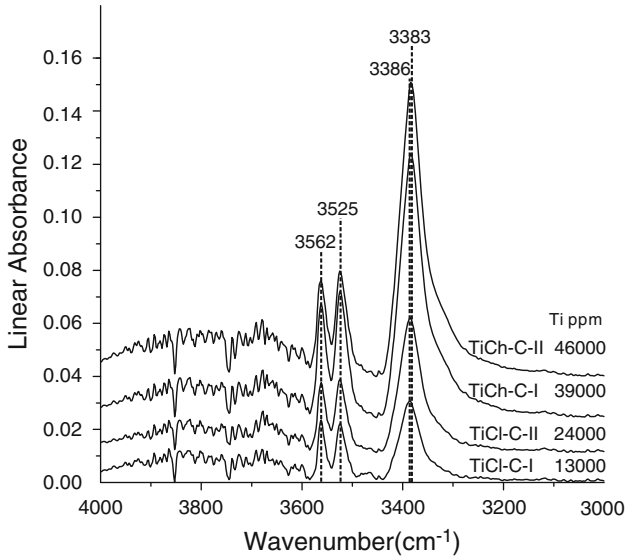

Fig. 4 Unpolarized ATR-FTIR spectra of Ti-clinohumite (TiCl-C) and Ti-chondrodite (TiCh-C). Group II contains higher amounts of Ti than group I for both minerals. The spectra represent the average of more than 20 analyses. Note that there is a small shift in the main band from 3,383 cm^{-1} in TiCh to 3,386 cm^{-1} in TiCl

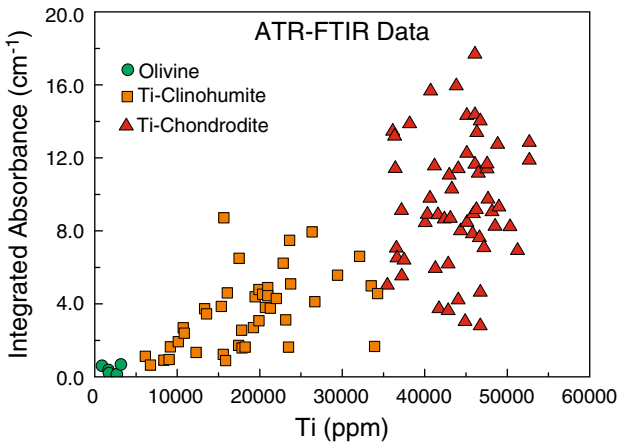

Fig. 5 Integrated absorbance of olivine, Ti-clinohumite, Ti-chondrodite measured by ATR-FTIR versus Ti content in these minerals

humite minerals was too strong, resulting in the saturation of the detector. Therefore, we changed the strategy and worked with inclusion-free, separated mineral grains from the same sample. Separated TiCh-C and TiCl-C grains were mounted in epoxy resin, and polished until the centres of the grains were exposed for ATR-FTIR, SEM and LA-ICP-MS analysis. Separated Ol-C grains were first measured using unpolarized transmission FTIR one by one, then mounted in epoxy resin, and further polished for LA-ICP-MS analyses.

Unpolarized ATR-FTIR measurement of randomly oriented Ti-clinohumite and Ti-chondrodite

56 TiCh-C, 43 TiCl-C and 5 yellow olivine randomly oriented grains were measured in ATR mode using the same method as applied for TiCl-M. Subsequently the grains were analysed in the same spot for Ti contents by SEM–EDS and LA-ICP-MS. The full dataset is presented in the Electronic Appendix Table 1. For an assessment of the IR spectra, the analysed grains were pooled into low Ti groups (13,000 ppm for TiCl-C-I; 39,000 ppm for TiCh-C-I) and high Ti groups (24,000 ppm for TiCl-C-II; 46,000 ppm for TiCh-C-II). The average spectra from these four groups are shown in Fig. 4.

Both TiCl-C-I and TiCl-C-II have three main bands at 3,562, 3,525 and 3,386 cm^{-1}. The bands at 3,562 and 3,525 cm^{-1} are sharp and similar in intensity, whereas the 3,386 cm^{-1} band has a shoulder and a stronger intensity than the bands at higher wavenumber. The absorbance intensity of TiCl-C-II is higher than that in TiCl-C-I. The linear absorbance ratio of 3,386 and 3,525 cm^{-1} is 1.4–1.9.

The main bands of TiCh-C are at 3,562, 3,525, 3,383 cm^{-1}, at almost the same position as in TiCl-C. The dominant band at 3,383 cm^{-1} in TiCh-C is shifted to slightly lower values compared to TiCl-C. Also, the linear absorbance ratio of 3,383 and 3,525 cm^{-1} in TiCh-C is 2.1–2.8, significantly higher than in TiCl. Both these characteristics are in agreement with the results presented in Hermann et al. (2007), indicating that these are likely general features that permit to distinguish between Ti-chondrodite and Ti-clinohumite on the basis of characteristic IR spectra. TiCh-C-II has a stronger absorbance than TiCh-C-I, and TiCh-C has higher linear absorbance than TiCl-C. Figure 5 shows the relation between the measured integrated absorbance from the ATR-FTIR measurements and the Ti contents for each grain. There is a broad positive correlation between Ti contents and absorbance.

Unpolarized transmission IR measurement of randomly oriented Ol-C

The separated clear olivines were relatively small and were placed on a copper grid with a 100-μm mesh that was attached to a sample holder and analysed by unpolarized transmission FTIR. After the FTIR analyses, the grains were placed on double sided tape and mounted in epoxy, polished until the centre of the grains was exposed and analysed with LA-ICP-MS.

For the quantification of the absorbance in FTIR measurements, the thickness of the sample must be known. Matveev and Stachel (2007) published a method to calculate the thicknesses of individual olivine grains using the integrated area of the second-order silica overtones between 1,625 and 2,150 cm^{-1} in olivine. A linear fit forced through the origin gives $A_{\text{int-overtone}} = 0.6366 * t_{\text{smp}}$,

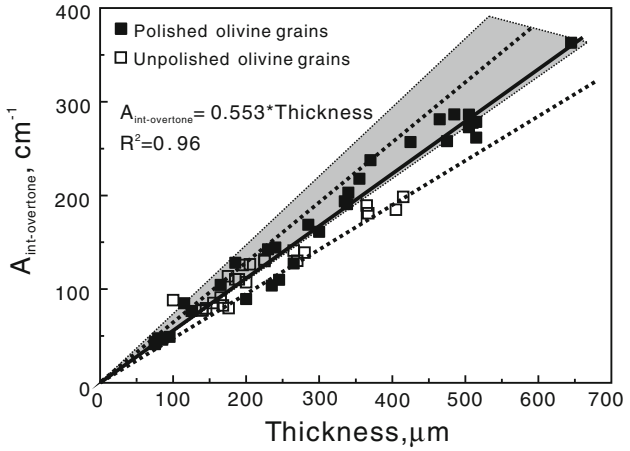

Fig. 6 Integrated absorbance of second-order Si–O overtones (from 1,625 to 2,150 cm^{-1}) versus thickness of the polished and unpolished olivine grains. The linear regression, which is forced through the origin, is shown with a *black solid line*. The linear equation is used for calculating the thickness of Ol-C. The error is about ±15 % (*dotted lines*). The results of Matveev and Stachel (2007) are shown for comparison (*grey shadow*)

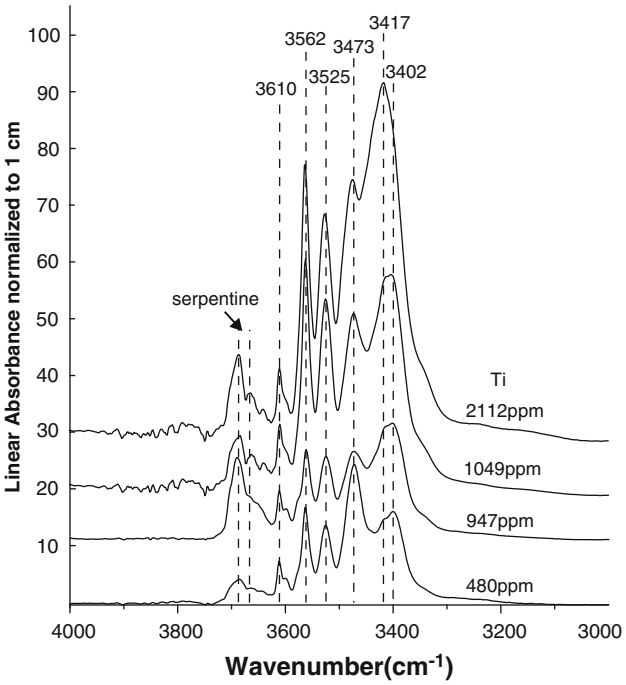

Fig. 7 Selected unpolarized FTIR spectra of olivine with different Ti contents (shown beside the spectra). All spectra were normalized to 1 cm sample thickness. The main bands are labelled

where $A_{\text{int-overtone}}$ is the integrated area of the second-order silica overtones between 1,625 and 2,150 cm^{-1} and t_{smp} is the sample thickness in micrometres. The method estimates the sample thickness with a claimed accuracy of ±15 %. We tested this method by measuring both polished and unpolished randomly oriented olivine grains with unpolarized FTIR and measured their thickness with the Mitutoyo machinist's digital indicator. The spectra were processed using the same method as applied for TiCl-C, TiCh-C and Ol-C. The integrated absorbance of the second-order Si–O overtone indeed varies linearly with the thickness of olivine grains (Fig. 6). The best-fit linear regression forced through the origin returned a slightly different slope with $A_{\text{int-overtone}} = 0.553 * t_{\text{smp}}$. The thickness obtained with our empirical parameter is therefore 15 % larger than using the previous calibration from Matveev and Stachel (2007). In the following, we used this modified function to calculate the thickness of Ol-C.

Representative spectra of Ol-C with different Ti contents show five dominant bands at 3,610, 3,562, 3,525, 3,473 and 3,417–3,402 cm^{-1} (Fig. 7). The band near 3,700 cm^{-1} is attributed to serpentine. The intense bands at 3,562, 3,525 and 3,417–3,402 cm^{-1} are very similar to the bands observed in the Ti-chlinohumite and Ti-chondrodite suggesting the presence of lamellar defects in olivine. The linear absorbance of the 3,417–3,402 cm^{-1} band correlates strongly with the measured Ti contents of the olivine grains (Fig. 7). The bands at 3,610 and 3,473 cm^{-1} are related to hydrated Si vacancies (Lemaire et al. 2004; Berry et al. 2005). H in a Si vacancy associated with Ti (Ti-clinohumite point defect) produces characteristic bands at 3,572 and 3,525 cm^{-1} (Berry et al. 2005, 2007). The 3,525 cm^{-1} band overlaps directly with the Ti-clinohumite lamellae band and thus is not diagnostic. There is a small shoulder on the high wavenumber side of the 3,562 cm^{-1} band indicating that a small amount of Ti-clinohumite point defects are present in the olivines. We could not observe any bands at 3,355 and 3,325 cm^{-1}, which are considered to be the water defect sites associated with Fe^{3+} and other trivalent cations (Berry et al. 2005, 2007). The integrated absorbance of Ol-C, normalized to 1 cm thickness using the Si overtones (Fig. 6), correlates positively with the Ti contents (Fig. 8a).

TEM observations in Ti-clinohumite

A TiCl-C grain associated with Ol-C and TiCh-C was chosen for the TEM study. Figure 9 shows a bright-field TEM image of a Ti-clinohumite grain that has been carefully aligned with the beam parallel to the crystallographic *b*-axis of Ti-clinohumite. The image clearly shows layers with different unit cells. In the area with the larger spacing, we measured five repetitions with the distance of 6.948 nm, whereas in the small cell parameter area, the distance of five repetitions is 3.801 nm. Thus, the majority of the layers display a spacing of 13.9 Å along the *c*-axes whereas a small area in the centre of the analysed regions displays a significantly shorter repeat distance of 7.6 Å. Based on X-ray diffraction data (Gibbs et al. 1970; Robinson et al. 1973; Yamamoto and Akimoto 1974; Aoki

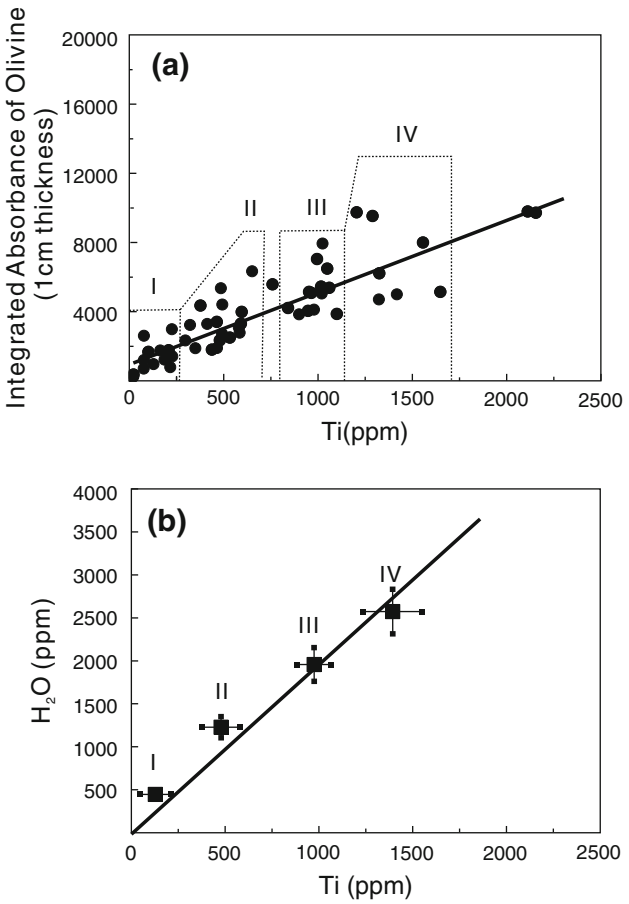

Fig. 8 **a** Integrated absorbance of olivine analysed by unpolarized FTIR versus Ti contents measured by LA-ICP-MS. All the data were divided into four groups as group I, II, III, IV, respectively, based on similar Ti contents. **b** Water content based on total absorbance of randomly oriented grains of the four groups of olivine as a function of the average Ti content. *Error bars* refer to 1 standard deviation from the multiple Ti analyses and 10 % for the error on total absorbance from multiple analyses of randomly oriented grains

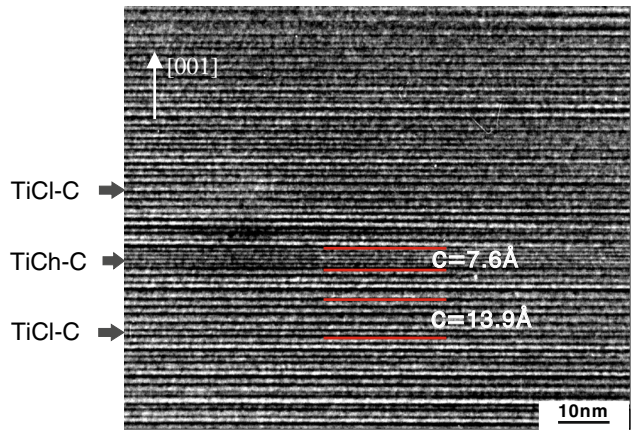

Fig. 9 TEM micrograph of a Ti-clinohumite region from the ion-thinned foil of serpentinized wehrlite (C11107), Tianshan, China, showing Ti-chondrodite lamellae intergrowth with Ti-clinohumite. The domains used to determine the length of the unit cell along the *c*-axes are indicted in *red*

et al. 1976), unit cell dimension of Ti-clinohumite and Ti-chondrodite is about 13.65–13.7 and 7.84-7.91 Å, respectively. Therefore, the observed structure is best explained by Ti-chondrodite lamellae interlayered in the Ti-clinohumite.

Discussion

Determination of water contents

The average unpolarized ATR-FTIR spectra of high and low Ti-clinohumite and chondrodite display a regular trend (Fig. 4). The average linear absorbance of the Ti-chondrodite is significantly higher than that of Ti-clinohumite and within the mineral groups, the higher Ti contents are related to higher absorbance. The path length of IR beam is the same for Ti-chondrodite and Ti-clinohumite and thus the obvious difference in absorbance between the two minerals translates directly to a difference in water contents. However, there is considerable scatter when the single analyses are plotted in a Ti versus absorbance diagram (Fig. 5). The IR absorbance in the humite minerals is anisotropic (Fig. 2, Electronic Appendix Figs. 3, 4) and thus the absorbance will depend on the orientation of the grains as well. To minimize this effect and in order to obtain the total absorbance, we pooled the TiCl-C analyses into four and the TiCh-C into five groups according to their Ti contents. The maximum unpolarized linear absorbance is well below 0.15 (Fig. 4) and thus the unpolarized quantification method to obtain total absorbance $A_{\text{total}} = -A_{\text{unpol}} * 3$ can be applied (Kovács et al. 2008; Sambridge et al. 2008). Water contents are then calculated using the Beer–Lambert Law (1) and employing our determined absorption coefficient $k_{\text{TiCl}} = 0.125$ ppm cm^2 (Table 3). The resulting relation between water contents and Ti concentration of the humite minerals is shown in Fig. 10. There is a strong positive correlation between Ti contents and water in both Ti-chondrodite and Ti-clinohumite albeit with different slopes. According to the chemical formula of Ti-clinohumite $4((Mg, Fe)_2SiO_4)(Mg_{1-X}, Ti_X)O_{2X}(OH, F)_{2-2X}$, and Ti-chondrodite $2((Mg, Fe)_2SiO_4)(Mg_{1-X}, Ti_X)O_{2X}(OH, F)_{2-2X}$, the water content of these humite minerals should decrease with increasing Ti content as shown in Fig. 10. It is worth noting that none of the measured Ti-clinohumites and Ti-chondrodites from Changawuzi plot on the theoretical line for the solid solution. Therefore, the observed relation between Ti and water reflects mixing between olivine and humite minerals rather than a heterogeneous Ti and water concentration

Table 3 Titanium and water contents of different groups of Ti-clinohumite and Ti-chondrodite

Sample	TiO_2 (wt%)	Ti (ppm)		Average integrated absorbance (cm^{-1}) (AIA)	Total absorbance (cm^{-1}) (3*AIA)	t (μm)	k (ppm cm^2)	H_2O (ppm)
			SD					
Ti-clinohumite								
TiCl-C-1 (10)	1.61	9,663	2,263	1.7	5.2	1.25	0.125	5,210
TiCl-C-2 (10)	2.72	16,280	1,366	3.5	10.5	1.25	0.125	10,500
TiCl-C-3 (10)	3.36	20,110	964	3.8	11.4	1.25	0.125	11,400
TiCl-C-4 (13)	4.55	27,300	4,716	4.9	14.6	1.25	0.125	14,600
Ti-chondrodite								
TiCh-C-1 (10)	6.13	36,770	770	9.2	27.5	1.25	0.125	27,400
TiCh-C-2 (9)	6.86	41,100	742	9.1	27.2	1.25	0.125	27,200
TiCh-C-3 (10)	7.28	43,650	709	8.2	24.7	1.25	0.125	24,700
TiCh-C-4 (19)	7.74	46,395	807	10.4	31.3	1.25	0.125	31,300
TiCh-C-5 (8)	8.38	50,200	1,835	9.9	29.7	1.25	0.125	29,700

The number of grains analysed in each group is given in parenthesis

within the Ti-chondrodite and Ti-clinohumite. This distinction is only possible when water and Ti contents are measured independently.

The IR spectra of olivine display a strong band at ~3,400, 3,525 and 3,562 cm^{-1} (Fig. 7), that is characteristic for Ti-clinohumite (Fig. 4). Additionally there is a strong correlation between the intensity of absorption and Ti contents of the olivines (Fig. 8a). This provides evidence that clinohumite lamellae defects are the main contributor to the water in olivine. Recent work has shown that different defects in olivine may have different absorption coefficients (Kovács et al. 2010). Given that the principle absorbance in olivine is related to clinohumite lamellae defects, it is appropriate to use the absorption coefficient $k_{TiCl} = 0.125$ ppm cm^2 instead of 0.188 ppm cm^2, which is the absorption coefficient generally used for olivine (Bell et al. 2003), to calculate the water content in Ol-C. As with the humite analysis, the scatter in the integrated absorbance of the grains is partly related to the anisotropy of absorbance in olivine. The Ol-C was pooled into four groups with similar Ti contents (Fig. 8a) in order to determine the total absorbance from randomly oriented grains. The linear absorbance of olivine in groups II, III and IV was higher than 0.3 and thus the total absorbance from these averages might be underestimated (Kovács et al. 2008). The resulting water contents are high and range from 440 to 2,600 ppm H_2O and display a very systematic increase with increasing Ti contents (Fig. 8b; Table 4). The correlation line is forced to go through the origin. Small amounts of Si vacancy point defects are also manifested by the bands at 3,610 and 3,473 cm^{-1} and they might contribute small amounts of water unrelated to Ti. This could be an explanation for the observation that group I and II plot slightly above the correlation line.

Intergrowth between olivine and humite minerals

Under the microscope, olivine displays sharp-oriented, yellow lamellae providing strong evidence for an intergrowth of olivine and Ti-clinohumite (Fig. 1). This is supported by the IR spectra of these olivine (Fig. 7) that show striking similarities with Ti-clinohumite. Ti-clinohumite lamellae in olivine were reported from: (1) mantle xenoliths within the Buell Park kimberlite with an estimated P–T condition of 1,000 °C, 2–3 GPa (Aoki et al. 1976; Kitamura et al. 1987); (2) garnet peridotites at Cima di Gagnone, Central Alps (Risold et al. 2001) with a peak metamorphic conditions of 780 °C, 3 GPa (Scambelluri et al. 2014); (3) serpentinites in the Almirez Massif (Spain), which reached peak conditions of 670 °C, 1.6–1.9 GPa (López Sánchez-Vizcaíno et al. 2005, 2009; Padrón-Navarta et al. 2010); (4) olivine formed during the breakdown of Ti-clinohumite from an orthopyroxenite in Dabie Shan (China) with the peak metamorphic condition of 4.0 ± 1.0 GPa, 700 ± 50 °C (Liou and Zhang 1998; Jahn et al. 2003; Hermann et al. 2007). Olivines from the last setting were analysed by Hermann et al. (2007) with TEM and IR-spectroscopy demonstrating the link between the FTIR spectra and planar Ti-clinohumite defects. The FTIR spectra of olivines from Cima di Gagnone, Dabie Shan and Almirez Massif all display the same water (as OH) bands at 3,564, 3,525 and ~3,400 cm^{-1} as Ti-clinohumite (Hermann et al. 2007), in agreement with the result of this study.

The most interesting feature of the present study is the relationship between water and Ti in olivine and clinohumite. The observed variation in Ti-clinohumite (Fig. 10) is consistent with a simple intergrowth with olivine. However, the Ti-H_2O trend in olivine (Figs. 8b, 10) provides

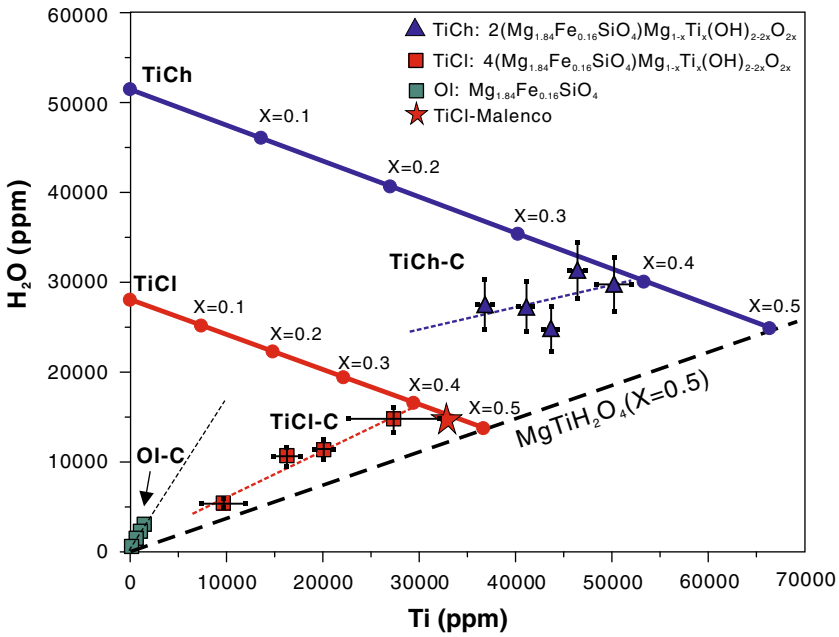

Fig. 10 Calculated water content in TiCh, TiCl and Ol based on total absorbance of randomly oriented grains as a function of measured Ti contents. The four data points of Ol-C are the same as in Fig. 8 and Table 4; four data points of TiCl-C and five data points of TiCh-C are the same data as in Fig. 5 and Table 3. Ideal Ti-chondrodite (*thick blue line*) and Ti-clinohumite (*thick red line*) were calculated based on the chemical formulae with various X_{Ti}. *Error bars* refer to 1 standard deviation from the multiple Ti analyses and 10 % for the error on total absorbance from multiple analyses of randomly oriented grains

Table 4 Titanium and water contents of different groups of olivine

Sample	Ti (ppm)		Average intergrated absorbance (cm^{-2}) (AIA)	Total absorbance (cm^{-2}) (3*AIA)	k (ppm cm^2)	C_{H2O} (ppm)
		SD				
Ol-I ($n = 13$)	128	82	1,180	3,540	0.125	442
Ol-II ($n = 18$)	478	100	3,280	9,840	0.125	1,230
Ol-III ($n = 13$)	972	91	5,234	15,702	0.125	1,960
Ol-IV ($n = 7$)	1,397	157	6,909	20,727	0.125	2,590

The number of grains analysed in each group is given in parenthesis

evidence that the Ti-clinohumite lamellae in olivine must have a significantly lower X of 0.19, than the macroscopic Ti-clinohumites with an $X = 0.41$. The calculated water content in olivine using the calibration of $k_{Ol} = 0.188$ ppm cm^2 (Bell et al. 2003) would be 50 % higher than what we used based on our newly determined absorption coefficient $k_{TiCl} = 0.125$ ppm cm^2 for lamellar defects in olivine. Hence, using the Bell calibration would make the X for the Ti-clinohumite lamellae in olivine even lower. This indicates that lower amounts of Ti are required to stabilize clinohumite planar defects in olivine than to stabilize the macroscopic Ti-clinohumite phase.

TEM images of Ti-clinohumites provide clear evidence for the intergrowth of Ti-clinohumite and Ti-chondrodite (Fig. 9). Such an intergrowth is impossible to detect with FTIR alone because the spectra of the two phases are so similar. However, the quantification of water and Ti supports such an intergrowth. The scatter of the five groups of Ti-chondrodite suggests that there is intergrowth with Ti-clinohumite as well as olivine. The Ti-chondrodite endmember has an approximate X between 0.35 and 0.40 (Fig. 10).

Implications for deep subduction of water

The investigated ultramafic rocks from Changawuzi are associated with eclogites and occur in an area where deep subduction of rocks to UHP conditions is documented (Zhang et al. 2003; Lü et al. 2008, 2009, 2012b; Lü and Zhang 2012; Yang et al. 2013). Ti-clinohumite lamellae in olivine have also been described from Almirez, Cima di Gagnone and Dabie shan (see above) that are all related to deeply subducted rocks. Mantle xenoliths from Buell Park that contain olivine with Ti-clinohumite lamellae come from the Colorado Plateau (Aoki et al. 1976; Kitamura et al. 1987), where xenoliths of subducted oceanic crust also have been described (Usui et al. 2006). Therefore, Ti-clinohumite lamellar defects in olivine seem to be a common feature in subducted ultramafic rocks.

In the investigated sample, olivine coexists with hydrous minerals such as Ti-clinohumite, Ti-chondrodite, chlorite and antigorite. Detail petrology and experimental work of these rocks, that will be discussed in detail elsewhere, indicate that olivine associated with Ti-chondrodite and antigorite formed at very high pressures of >3.6 GPa at temperatures of 520–550 °C, characteristic of cold subducted slabs. Interestingly, the Ti-clinohumite lamellae defects in olivine also occur in garnet peridotites of Cima di Gagnone (Risold et al. 2001; Hermann et al. 2007) that do not contain any of these hydrous phases. A recent study has shown that the Cima di Gagnone rocks originate from prograde dehydration of serpentinites during subduction at a similar pressure of ~3 GPa, but higher temperatures of 780–800 °C (Scambelluri et al. 2014). Rare relic Ti-clinohumite as well as olivine + ilmenite intergrowth typical for Ti-clinohumite breakdown is present in the garnet peridotites (Scambelluri et al. 2014). This indicates that water transport in lamellae within olivine is possible at conditions that exceed the stability of chlorite, antigorite and Ti-clinohumite. Therefore, olivines with Ti-clinohumite defects are able to transport water to greater depth in subducted ultramafic rocks than the hydrous phases.

The observed strong correlation between Ti and water can be used to estimate the capacity of ultramafic rocks to transport water in subduction zones beyond the breakdown of hydrous phases. Figure 10 shows that olivine with lamellae defect can transport the highest amount of water for a given Ti content, followed by Ti-clinohumite and Ti-chondrodite. If all the Ti is hosted in olivine, then about 1,660 ppm H_2O can be stored in the investigated wehrlite C11107 for the measured 480 ppm Ti. Harzburgite with typical 500 ppm Ti would have a similar maximum water storage capacity whereas lherzolites with up to 1,200 ppm Ti potentially could host even higher water contents. However, it is unlikely that these maximum water contents persist during further burial of ultramafic rocks within the subducted slab. The olivines at Cima di Gagnone contain also oriented ilmenite rods (Risold et al. 2001) that likely originate from the dehydration of Ti-clinohumite lamellae. Additionally, ilmenite occurs as accessory mineral (Scambelluri et al. 2014) and thus not all Ti is bound in hydrous olivine. Therefore, it seems plausible that small amounts of water are liberated continuously from dehydrating humite lamellae within olivine during subduction of ultramafic rocks. It is expected that with increasing temperature, point defects are becoming more abundant (Hermann et al. 2007). The strong link between Ti and water in olivine might still persist into regions where such point defects are dominant, as shown for the lithospheric mantle beneath Germany (Schmädicke et al. 2013), where H in point defects associated with Ti is the most important mode of water storage in the upper mantle leading to a correlation between water and Ti contents.

Conclusions

1. We applied attenuated total reflectance (ATR) FTIR to the investigation of the hydrous minerals Ti-clinohumite and Ti-chondrodite. The path length of IR light through these minerals is 1.25 μm using a Ge-tip ATR objective. The two humite minerals display similar IR bands at ~3,562, 3,525 and ~3,583–3,586 cm^{-1}, but Ti-chondrodite has a stronger absorbance than Ti-clinohumite and the ratio of linear absorbance between 3,583–3,586 and the 3,525 cm^{-1} bands is higher in Ti-chondrodite.
2. An absorption coefficient of 0.125 ppm cm^2 for Ti-clinohumite has been determined with polarized FTIR measurements of three perpendicular sections from a large Ti-clinohumite sample from Val Malenco, Italy, for which the water content has been determined previously.
3. Olivine from an UHP serpentinite in Tianshan, China, contains extensive Ti-Clinohumite lamellae. The measured Ti and H_2O contents of Ti-clinohumite and Ti-chondrodite provide evidence for an intergrowth of Ti-clinohumite with olivine and Ti-chondrodite with Ti-clinohumite and olivine.
4. The ratio of H_2O to Ti is highest in olivine, followed by Ti-chondrodite and Ti-clinohumite. The water content in olivines that contain Ti-clinohumite lamellae ranges from 440 to 2,590 ppm. Such olivine is likely to be stable even after the dehydration of antigorite and chlorite and could be an important carrier of water to the deeper mantle in subducted ultramafic rocks.

Acknowledgments We thank China Scholarship Council for supporting 12-month visiting study for T. T. Shen in Australia. We appreciate Mr Harri Kokkonen (ANU) for kind help with infrared sample preparation, Penny King (ANU) for infrared analysis and Jung Park (ANU) for LA-ICP-MS analysis. We thank Yi Cao (Seoul National University, Korea) for help with drawing Fig. 2 and Electronic Appendix Figs. 3, 4 in the paper. We also wish to thank Zeng Lü, Bin Xia, Renbiao Tao, Yang Xia in Peking University for fieldwork. We thank R. Stalder and I. Kovács for constructive reviews and J. Hoefs for efficient handling of the paper. JAPN has been supported by a EU-FP7-funded Marie Curie postdoctoral grant under contract agreement PIOF-GA-2010-273017. This work has been financially supported by the Australian Research Council and NSF of China (Grants 41272069, 41121062, 41330210).

References

Aizawa Y, Barnhoorn A, Faul UH, Fitz Gerald JD, Jackson I, Kovács I (2008) Seismic properties of Anita Bay dunite: an exploratory study of the influence of water. J Petrol 49:841–855

Aoki K, Fujino K, Masaki A (1976) Titanochondrodite and titanoclinohumite derived from the upper mantle in the Buell Park Kimberlite, Arizona, USA. Contrib Miner Petrol 56:243–253

Bell DR, Rossman GR (1992) Water in Earth's Mantle: the role of nominally anhydrous minerals. Science 255:1391–1397

Bell DR, Ihinger PD, Rossman GR (1995) Quantitative analysis of trace OH in garnet and pyroxenes. Am Miner 80:465–474

Bell DR, Rossman GR, Maldener J, Endisch D, Rauch F (2003) Hydroxide in olivine: a quantitative determination of the absolute amount and calibration of the IR spectrum. J Geophy Res 108:2105. doi:10.1029/2001JB000679

Berry AJ, Hermann J, O'Neill HSC, Foran GJ (2005) Fingerprinting the water site in mantle olivine. Geology 33:869–872. doi:10.1130/G21759.1

Berry AJ, O'Neill HSC, Hermann J, Scott DR (2007) The infrared signature of water associated with trivalent cations in olivine. Earth Planet Sci Lett 261:134–142

Costa F, Chakraborty S (2008) The effect of water on Si and O diffusion rates in olivine and implications for transport properties and processes in the upper mantle. Phys Earth Planet Inter 166:11–29

Demouchy S, Jacobsen SD, Gaillard F, Stern CR (2006) Rapid magma ascent recorded by water diffusion profiles in mantle olivine. Geology 34:429–432

Denis CMM, Demouchy S, Shaw CSJ (2013) Evidence of dehydration in peridotites from Eifel Volcanic Field and estimates of the rate of magma ascent. J Volcanol Geoth Res 258:85–99

Dixon JE, Dixon TH, Bell DR, Malservisi R (2004) Lateral variation in upper mantle viscosity: role of water. Earth Planet Sci Lett 222:451–467

Gibbs GV, Ribbe PH, Anderson CP (1970) The crystal structures of the humite minerals. II. Chondrodite. Am Miner 55:1183–1194

Grant KJ, Brooker RA, Kohn SC, Wood BJ (2007a) The effect of oxygen fugacity on hydroxyl concentrations and speciation in olivine: implications for water solubility in the upper mantle. Earth Planet Sci Lett 261:217–229

Grant K, Ingrin J, Lorand JP, Dumas P (2007b) Water partitioning between mantle minerals from peridotite xenoliths. Contrib Miner Petrol 154:15–34

Hermann J, Fitz Gerald JD, Malaspina N, Berry AJ, Scambelluri M (2007) OH-bearing planar defects in olivine produced by the breakdown of Ti-rich humite minerals from Dabie Shan (China). Contrib Miner Petrol 153:417–428

Hirth G, Kohlstedt DL (1996) Water in the oceanic upper mantle: implications for rheology, melt extraction and the evolution of the lithosphere. Earth Planet Sci Lett 144:93–108

Ingrin J, Skogby H (2000) Hydrogen in nominally anhydrous upper-mantle minerals: concentration levels and implications. Eur J Miner 12:543–570

Jahn B, Fan Q, Yang JJ, Henin O (2003) Petrogenesis of the Maowu pyroxenite-eclogite body from the UHP metamorphic terrane of Dabieshan: chemical and isotopic constraints. Lithos 70:243–267

Karato S (2006) Remote sensing of hydrogen in Earth's mantle. In: Keppler H, Smyth JR (eds) Water in nominally anhydrous minerals. Mineralogical Society of America and Geochemical Society, Reviews in Mineralogy and Geochemistry 62, pp 343–375

Karato S, Jung H (1998) Water, partial melting and the origin of the seismic low velocity and high attenuation zone in the upper mantle. Earth Planet Sci Lett 157:193–207

Kitamura M, Kondoh S, Morimoto N, Miller GH, Rossman GR, Putnis A (1987) Planar OH-bearing defects in mantle olivine. Nature 328:143–145

Kovács I, Hermann J, O'Neill HSC, Gerald JF, Sambridge M, Horváth G (2008) Quantitative absorbance spectroscopy with unpolarized light: part II. Experimental evaluation and development of a protocol for quantitative analysis of mineral IR spectra. Am Miner 93:765–778

Kovács I, O'Neill HSC, Hermann J, Hauri EH (2010) Site-specific infrared O–H absorption coefficients for water substitution into olivine. Am Miner 95:292–299

Kovács I, Green DH, Rosenthal A, Hermann J, O'Neill HSC, Hibberson WO, Udvardi B (2012) An experimental study of water in nominally anhydrous minerals in the upper mantle near the water-saturated solidus. J Petrol 53:2067–2093

Lemaire C, Kohn SC, Brooker RA (2004) The effect of silica activity on the incorporation mechanisms of water in synthetic forsterite: a polarised infrared spectroscopic study. Contrib Miner Petrol 147:48–57

Li XP, Zhang L, Wei C, Ai Y, Chen J (2007) Petrology of rodingite derived from eclogite in western Tianshan, China. J Metamorph Geol 25:363–382

Li ZXA, Lee CTA, Peslier AH, Lenardic A, Mackwell SJ (2008) Water contents in mantle xenoliths from the Colorado Plateau and vicinity: implications for the mantle rheology and hydration-induced thinning of continental lithosphere. J Geophy Res 113:B09210. doi:10.1029/2007JB005540

Libowitzky E, Rossman GR (1996) Principles of quantitative absorbance measurements in anisotropic crystals. Phys Chem Miner 23:319–327

Liou JG, Zhang RY (1998) Petrogenesis of an ultrahigh-pressure garnet-bearing ultramafic body from Maowu, Dabie Mountains, east-central China. Isl Arc 7:115–134

López Sánchez-Vizcaíno V, Trommsdorff V, Gómez-Pugnaire MT, Garrido CJ, Müntener O, Connolly JAD (2005) Petrology of titanian clinohumite and olivine at the high-pressure breakdown of antigorite serpentinite to chlorite harzburgite (Almirez Massif, S. Spain). Contrib Miner Petrol 149:627–646

López Sánchez-Vizcaíno V, Gómez-Pugnaire MT, Garrido CJ, Padrón-Navarta JA, Mellini M (2009) Breakdown mechanisms of titanclinohumite in antigorite serpentinite (Cerro del Almirez massif, S. Spain): a petrological and TEM study. Lithos 107:216–226

Lowenstern JB, Pitcher BW (2013) Analysis of H_2O in silicate glass using attenuated total reflectance (ATR) micro-FTIR spectroscopy. Am Miner 98:1660–1668

Lü Z, Zhang LF (2012) Coesite in the eclogite and schist of the Atantayi Valley, southwestern Tianshan, China. Chinese Sci Bull 57:1467–1472

Lü Z, Zhang LF, Du JX, Bucher K (2008) Coesite inclusions in garnet from eclogitic rocks in western Tianshan, northwest China: convincing proof of UHP metamorphism. Am Miner 93:1845–1850

Lü Z, Zhang L, Du J, Bucher K (2009) Petrology of coesite-bearing eclogite from Habutengsu Valley, western Tianshan, NW China and its tectonometamorphic implication. J Metamorph Geol 27:773–787

Lü Z, Bucher K, Zhang L, Du J (2012a) The Habutengsu metapelites and metagreywackes in western Tianshan, China: metamorphic evolution and tectonic implications. J Metamorph Geol 30:907–926

Lü Z, Zhang LF, Du JX, Yang X, Tian ZL, Xia B (2012b) Petrology of HP metamorphic veins in coesite-bearing eclogite from western Tianshan, China: fluid processes and elemental mobility during exhumation in a cold subduction zone. Lithos 136–139:168–186

Matveev S, Stachel T (2007) FTIR spectroscopy of OH in olivine: a new tool in kimberlite exploration. Geochim Cosmochim Acta 71:5528–5543

Matveev S, O'Neill HSC, Ballhaus C, Taylor WR, Green DH (2001) Effect of silica activity on OH^- IR spectra of olivine: implications for low-aSiO_2 mantle metasomatism. J Petrol 42:721–729

Mosenfelder JL, Rossman GR (2013a) Analysis of hydrogen and fluorine in pyroxenes: I. Orthopyroxene. Am Miner 98:1026–1041

Mosenfelder JL, Rossman GR (2013b) Analysis of hydrogen and fluorine in pyroxenes: II. Clinopyroxene. Am Miner 98:1042–1054

Mosenfelder JL, Deligne NI, Asimow PD, Rossman GR (2006) Hydrogen incorporation in olivine from 2–12 GPa. Am Miner 91:285–294

Otsuka K, Karato S (2011) Control of the water fugacity at high pressures and temperatures: applications to the incorporation mechanisms of water in olivine. Phys Earth Planet Inter 189:27–33

Padrón-Navarta JA, Hermann J, Garrido CJ, López Sánchez-Vizcaíno V, Gómez-Pugnaire MT (2010) An experimental investigation of antigorite dehydration in natural silica-enriched serpentinite. Contrib Miner Petrol 159:25–42

Padrón-Navarta JA, Hermann J, O'Neill HSC (2014) Site-specific hydrogen diffusion rates in Forsterite. Earth Planet Sci Lett 392:100–112

Paterson M (1982) The determination of hydroxyl by infrared absorption in quartz, silicate glass and similar materials. Bull Miner 105:20–29

Peslier AH, Luhr JF (2006) Hydrogen loss from olivines in mantle xenoliths from Simcoe (USA) and Mexico: mafic alkalic magma ascent rates and water budget of the sub-continental lithosphere. Earth Planet Sci Lett 242:302–319

Peslier AH, Woodland AB, Wolff JA (2008) Fast kimberlite ascent rates estimated from hydrogen diffusion profiles in xenolithic mantle olivines from southern Africa. Geochim Cosmochim Acta 72:2711–2722

Risold AC, Trommsdorff V, Grobéty B (2001) Genesis of ilmenite rods and palisades along humite-type defects in olivine from Alpe Arami. Contrib Miner Petrol 140:619–628

Robinson K, Gibbs GV, Ribbe PH (1973) The crystal structure of the humite minerals. IV. Clinohumite and titanoclinohumite. Am Miner 58:43–49

Sambridge M, Fitz Gerald J, Kovács I, O'Neill HSC, Hermann J (2008) Quantitative absorbance spectroscopy with unpolarized light: part I. Physical and mathematical development. Am Miner 93:751–764

Scambelluri M, Pettke T, Rampone E, Godard M, Reusser E (2014) Petrology and trace element budgets of high pressure peridotites indicate subduction dehydration of pristine serpentinites (Cima Di Gagnone, Central Alps, Switzerland). J Petrol 55:459–498

Schlechter E, Stalder R, Behrens H (2012) Electrical conductivity of H-bearing orthopyroxene single crystals measured with impedance spectroscopy. Phys Chem Miner 39:531–541

Schmädicke E, Gose J, Witt-Eickschen G, Brätz H (2013) Olivine from spinel peridotite xenoliths: hydroxyl incorporation and mineral composition. Am Miner 98:1870–1880

Schmidt MW, Poli S (1998) Experimentally based water budgets for dehydrating slabs and consequences for arc magma generation. Earth Planet Sci Lett 163:361–379

Shen TT, Zhang LF, Li XP (2012) Geochemical characteristics of rodingite derived from eclogite in western Tianshan, Xinjiang, China and its implication of subduction zone fluid. Acta Petrol Sin 28:2235–2249 (In Chinese with English Abstract)

Smyth JR, Frost DJ, Nestola F, Holl CM, Bromiley G (2006) Olivine hydration in the deep upper mantle: effects of temperature and silica activity. Geophys Res Lett 33:L1530115. doi:10.1029/2006GL026194

Soustelle V, Tommasi A, Demouchy S, Ionov DA (2010) Deformation and fluid-rock interaction in the supra-subduction mantle: microstructures and water contents in peridotite xenoliths from the Avacha Volcano, Kamchatka. J Petrol 51:363–394

Spandler C, Pirard C (2013) Element recycling from subducting slabs to arc crust: a review. Lithos 170–171:208–223

Stalder R (2004) Influence of Fe, Cr and Al on hydrogen incorporation in orthopyroxene. Eur J Miner 16:703–711

Tenner TJ, Hirschmann MM, Withers AC, Ardia P (2012) H_2O storage capacity of olivine and low-Ca pyroxene from 10 to 13 GPa: consequences for dehydration melting above the transition zone. Contrib Miner Petrol 163:297–316

Tian ZL, Wei CJ (2013) Metamorphism of ultrahigh-pressure eclogites from the Kebuerte Valley, South Tianshan, NW China: phase equilibria and P-T path. J Metamorph Geol 31:281–300

Trommsdorff V, Evans BW (1974) Alpine metamorphism of peridotitic rocks. Schweiz Miner Petrogr Mitt 54:333–352

Trommsdorff V, Evans BW (1980) Titanian Hydroxyl-clinohumite: formation and breakdown in antigorite rocks (Malenco, Italy). Contrib Miner Petrol 72:229–242

Ulmer P, Trommsdorff V (1995) Serpentinite stability to mantle depths and subduction related magmatism. Science 268:858–861

Usui T, Nakamura E, Helmstaedt H (2006) Petrology and geochemistry of eclogite xenoliths from the Colorado Plateau: implications for the evolution of subducted oceanic crust. J Petrol 47:929–964

Walker AM, Hermann J, Berry AJ, O'Neill HSC (2007) Three water sites in upper mantle olivine and the role of titanium in the water weakening mechanism. J Geophy Res 112:B5211. doi:10.1029/2006JB004620

Weiss M (1997) Clinohumites: a field and experimental study, PhD thesis ETH Zürich, p 168

Xia QK, Hao YT, Li P, Deloule E, Coltorti M, Dallai L, Yang XZ, Feng M (2010) Low water content of the Cenozoic lithospheric mantle beneath the eastern part of the North China Craton. J Geophy Res 115:B07207. doi:10.1029/2009JB006694

Yamamoto K, Akimoto S (1974) High pressure and high temperature investigations in the system $MgO–SiO_2–H_2O$. J Solid State Chem 9:187–195

Yang X, Zhang LF, Tian ZL, Bader T (2013) Petrology and U-Pb zircon dating of coesite-bearing metapelite from the Kebuerte Valley, western Tianshan, China. J Asian Earth Sci 70–71:295–307

Zhang LF, Ellis DJ, Jiang WB (2002) Ultrahigh-pressure metamorphism in western Tianshan, China: part I. Evidence from inclusions of coesite pseudomorphs in garnet and from quartz exsolution lamellae in omphacite in eclogites. Am Miner 87:853–860

Zhang L, Ellis DJ, Arculus RJ, Jiang W, Wei CJ (2003) 'Forbidden zone' subduction of sediments to 150 km depth-the reaction of dolomite to magnesite + aragonite in the UHPM metapelites from western Tianshan, China. J Metamorph Geol 21:523–529

Zhang LF, Du JX, Lü Z, Yang X, Gou LL, Xia B, Chen ZY, Wei CJ, Song SG (2013) A huge oceanic-type UHP metamorphic belt in southwestern Tianshan, China: peak metamorphic age and PT path. Chinese Sci Bull 58:4378–4383

Zhao YH, Ginsberg SB, Kohlstedt DL (2004) Solubility of hydrogen in olivine: dependence on temperature and iron content. Contrib Miner Petrol 147:155–161